Purdue University

## Purdue e-Pubs

# Experimental Quantification of the Thermodynamic and Mechanical Losses of an oil-injected and economized 4/6 twin-screw compressor

Abhignan Saravana

Haotian Liu

Eckhard A. Groll

Davide Ziviani

Follow this and additional works at: https://docs.lib.purdue.edu/icec

# Experimental Quantification of the Thermodynamic and Mechanical Losses of an oil-injected and economized 4/6 twin-screw compressor

**Abhignan SARAVANA**[1*], **Haotian LIU**[1], **Eckhard A. GROLL**[1], **Davide ZIVIANI**[1]

[1] Ray W. Herrick Laboratories, School of Mechanical Engineering, Purdue University
West Lafayette, 47907-2099, USA
saravan0@purdue.edu; liu1460@purdue.edu; groll@purdue.edu; dziviani@purdue.edu

* Corresponding Author

## ABSTRACT

Oil-injected twin-screw compressors are widely employed in many commercial and industrial applications because of their high efficiency and reliability. Although extensive literature on modeling techniques applied to twin-screw machines exists, researchers are continuously developing models to capture advanced physical phenomena occurring during the compression process (e.g., mass and heat transfer mechanisms) as well as analyze the mechanical behavior of the compressor (e.g., rotordynamics, bearing loads, variation of clearance gaps). To validate these models, detailed experimental data is needed to capture the in-chamber compression process as well as mechanical loads.

This paper presents the results of extensive experimental testing of a 4/6 oil-injected twin-screw compressor with slide-valve part-load modulation and economization. The compressor has been equipped with high-frequency pressure sensors, load-cells at the bearings and torque sensor on the main rotor. Indicated diagrams are analyzed to experimentally quantify the various losses, and the impact of compressor operating conditions on performance is discussed at full-load and part-load.

## 1. INTRODUCTION

Oil injected twin-screw compressors are widely used in various industrial applications due to their reliability and high efficiencies, as well as the ability to operate at a wide range of flow rates and pressure ratios. However, the performance of these compressors under different conditions depends on a variety of thermodynamic factors (e.g., flow losses) and design considerations (e.g., gap clearances, bearings, port shape). Therefore, it is important to conduct thermodynamic analyses of the performance of these positive displacement machines and quantify both flow and mechanical losses.

Several research efforts have been conducted on analyzing and predicting the performance of twin-screw compressors. For instance, Haughland (1990) presented a method for pressure indication via five pressure transducers strategically located on the compressor casing. Stosic *et al.* (1991) analyzed the indicator diagrams of the oil-flooded twin-screw air compressor based on experimental and theoretical results. Jonsson (1990) explored an improvement to the twin-screw compressor setup using economizers with the help of simulation programs. This was later followed up by Wu *et al.* (2004) when they used indicator diagrams to investigate the effects of the super feed pressure together with economizer through experiments. They also developed a theoretical mathematical model for calculating the indicator diagram of twin screw refrigeration compressor by analyzing geometric parameters of the rotors (Huagen *et al.*, 2004). Seshaiah *et al.* (2019) performed a deeper analysis on thermodynamic performance parameters of twin screw air compressors such as efficiency, delivery rate and the heat of compression of the compressors. More recently, Shizhong *et al.* (2021) developed a test rig to test variable speed, variable slide valve configuration twin screw compressors and conducted noise analysis and indicated power calculation with the help of indicator diagrams.

Despite the numerous studies on twin-screw compressors, experimental investigations on mechanical losses are still limited (*e.g.*, Hou *et al.* (2017)). To quantify the mechanical losses associated with bearing frictional losses and other rotating parts (e.g., shaft seals), the indicated power must be measured along with male shaft torques and loads at the bearings. Forces decompositions and moments balance equations must be employed to close the mechanical analysis of the twin-screw compression process.

In this work, a 4/6 oil-injected twin-screw compressors that was previously instrumented (Salts *et al.* (2019)) has been used to collect experimental data at both full and part load conditions with and without economization. The twin screw compressor is equipped with axial force cells, static and dynamic pressure transducers, temperature measurements and torque sensors. The dynamic pressure transducers have been used to construct the indicator diagram and a mathematical model has been developed to compute indicated power and breakdown of the compression losses. The indicator diagrams are further analyzed to estimate thermodynamic and mechanical losses by comparing suction, compression, and discharge losses at every operating condition as well as computing isentropic, volumetric, mechanical and polytropic efficiencies.

## 2. TWIN-SCREW COMPRESSOR MODELS

### 2.1 Geometry
An open-drive twin-screw compressor with a 4/6 rotor configuration model has been identified as the unit to be modelled and tested as part of this study. The main geometry parameters of the rotors are reported Table 1. Detailed information regarding the rotor profiles can be found in a previous study conducted by the authors (Salts *et al.*, 2019).

**Table 1 – Screw rotor main geometric parameters.**

| Parameter | Value |
|---|---|
| Theoretical displacement | 0.90402 ft$^3$/rev (25599 cm$^3$/rev) |
| Compressor volume ratio | 2.0-4.1 |
| Rotor wrap angle, $\varphi_w$ | 325° |
| Male rotor lead (right hand helix) | 752 mm (29.6063 in) |
| Female rotor lead (left hand helix) | 1128 mm (44.4094 in) |
| Male lobes, $z_1$ | 4 |
| Female lobes, $z_2$ | 6 |
| Center distance, $A_{O_1O_2}$ | 222 mm |
| Rotor length, L | 679.20 mm |
| L/D$_m$ | 2.40 |

### 2.2 Test Matrix
The test matrix consisted of various operating conditions with a wide range of parameters, including suction and discharge pressure, volume ratio, load capacity dictated by the slide valves and slide stops as well as rotational speed. These parameters control the thermodynamic performance of the twin-screw compressor as is discussed in later sections. Table 2 reports Test #2 as a reference case to showcase the calculations, but the complete summary of all the test conditions can be found in Appendix A. To be noted is that the discharge mass flow rate includes the oil injected during the compression process.

**Table 2: Test matrix for Test #2 as a reference case**

| Test | RPM | $P_{SUC}$ (psi) | $P_{DIS}$ (psi) | Volume Ratio | Load | $\dot{m}_{suc}$ (lbm/min) | $\dot{m}_{dis}$ (lbm/min) |
|---|---|---|---|---|---|---|---|
| 2 | 1800 | 25 | 175 | 4.1 | 100 | 175.803 | 178.747 |

### 2.3 Models for Power Calculation
The indicated work of a compressor is calculated as the area covered by the suction, discharge, and compression curve as a function of volume of the chamber. The losses (e.g., flow and heat transfer losses) are then calculated by comparing the experimental indicator diagram with the ideal adiabatic polytropic compression process. The polytropic coefficient varies with the experimental conditions so that

$$P_{dis}V_{dis}^\gamma = P_{suc}V_{suc}^\gamma = const \tag{1}$$

where $P_{dis}$, $V_{dis}$, $P_{suc}$, $V_{suc}$ are suction and discharge pressures and volumes respectively and $\gamma$ is the polytropic coefficient. The ideal curve is projected between the two points of suction and discharge, keeping the above condition

and the polytropic coefficient is estimated using the Equation 1. For an isothermal compression process, Equation 1 reduces to $P_{suc}V_{suc} = const$.

The flow losses are computed as a comparison of the experimental indicator diagram to the ideal polytropic compression curve. They are compartmentalized into the three sections of suction, discharge and compression and individually computed. Equation 2-4 describe the calculation of suction, compression, and discharge losses respectively,

$$W_{suc,loss} = \int_0^{V_{max}} P_{exp,suc}\, dV - P_{suc}(V_{max}) \tag{2}$$

$$W_{comp,loss} = \int_{V_{max}}^{V_{dis}} P_{exp,comp}\, dV - \int_{V_{max}}^{V_{dis}} \frac{P_{suc}V_{suc}^{\gamma}}{V\gamma}\, dV \tag{3}$$

$$W_{dis,loss} = \int_{V_{dis}}^{0} P_{exp,dis}\, dV + P_{dis}(V_{dis}) \tag{4}$$

where $W_{dis,loss}$, $W_{comp,loss}$, $W_{suc,loss}$ are work losses pertaining to the discharge, compression, and suctions phases, respectively. $V_{max}$ is the volume at which the suction closes and there is no more refrigerant entering, while $V_{dis}$ is the final volume at which discharge occurs. The ratio of $V_{max}$ to $V_{dis}$ is the volume ratio. $P_{exp}$ is the polynomial spline fit on the experimental pressure curve with the volume as the independent variable. This is obtained from processing both the pressure and volume crank angle data obtained from the transducers as explained in the next sections.

The indicated work is therefore a sum of suction, discharge, and compression work as given in Equation 5. The indicated work calculated from the diagram is for one compression chamber. Hence, the computation of indicated power from indicated work is described by Equation 6.

$$W_{ind} = \int_0^{V_{max}} P_{exp,suc}\, dV + \int_{V_{max}}^{V_{dis}} P_{exp,comp}\, dV + \int_{V_{dis}}^{0} P_{exp,dis}\, dV \tag{5}$$

$$\dot{W}_{ind} = \frac{W_{ind}\, N_1\, z_1}{60} \tag{6}$$

where $W_{ind}$ and $\dot{W}_{ind}$ represent indicated work and indicated power respectively, $N_1$ represents the male rotor rotational speed in RPM and $z_1$ stands for number of male rotor lobes. The isentropic efficiency, volumetric efficiency, mechanical efficiency and polytropic efficiency can therefore be calculated using Equations 7 and 8.

$$\eta_{isen} = \frac{\dot{W}_{isen}}{\dot{W}_{ind}} \qquad\qquad \eta_{vol} = \frac{\dot{m}_{suc}}{\rho_{suc} * V_{chamber} * N_1} \tag{7}$$

$$\eta_{mech} = \frac{\dot{W}_{ind}}{\dot{W}_{shaft}} \qquad\qquad \eta_{poly} = \frac{\dot{W}_{poly}}{\dot{W}_{ind}} \tag{8}$$

where $\eta_{isen}$, $\eta_{vol}$, $\eta_{mech}$, $\eta_{poly}$ represent isentropic, volumetric, mechanical, polytropic efficiencies respectively, $\dot{W}_{isen}$, $\dot{m}_{suc}$, $\dot{W}_{shaft}$, $\dot{W}_{poly}$ represent isentropic power, suction mass flow rate, shaft power and polytropic power respectively. The shaft power is obtained as a single value from experiments whereas polytropic power is obtained by computing pressure volume work for the polytropic curve and summing it over all the compression chambers similar to the indicated power calculation. Lastly, the isentropic power for an ideal gas is computed as:

$$\dot{W}_{isen} = \left(\frac{\dot{m}_{suc}}{60}\right)\left(\frac{\gamma}{\gamma-1}\right) R\, T_{suc} \left(\left(\frac{P_{dis}}{P_{suc}}\right)^{\frac{\gamma-1}{\gamma}} - 1\right) \tag{9}$$

## 3. EXPERIMENTAL SETUP

There are two general methods for recording the indicator diagrams in an oil-flooded twin-screw compressor. One method where several pressure sensors are placed at consecutive positions within the housing that record data continuously. This data from the different sensors is then combined to produce one continuous pressure curve. Stosic *et al.* (1991) and Haugland (1990) described this method in their papers. The other method uses only one sensor, which is embedded into the groove at the root of the female rotor on the discharge side, to measure the whole working process, as described by Miyoshi (1992). In this case, the pressure signal is led out of the compressor through a slip ring. A highly accurate indicator diagram can be obtained through this process. The method used within this study involves the setup with pressure sensors placed along the rotor housing to record continuous data.

Five dynamic piezo electric pressure transducers are installed along the female rotor as shown in Figures 1a) and 1b). All sensors are installed using externally drilled and tapped holes, which ensures proper sealing and allows ease of maintenance. The sampling rate is determined by the compressor RPM and sensor with the shortest angle of rotation between opening and closing angle. For example, if sensor #1 has 50° of rotation between its opening and closing angle and the compressor operates at 6000 RPM, the minimum sampling rate of 1440 Hz is required to ensure that the sample is taken every 25° of rotation completing roughly 2 samples per working chamber.
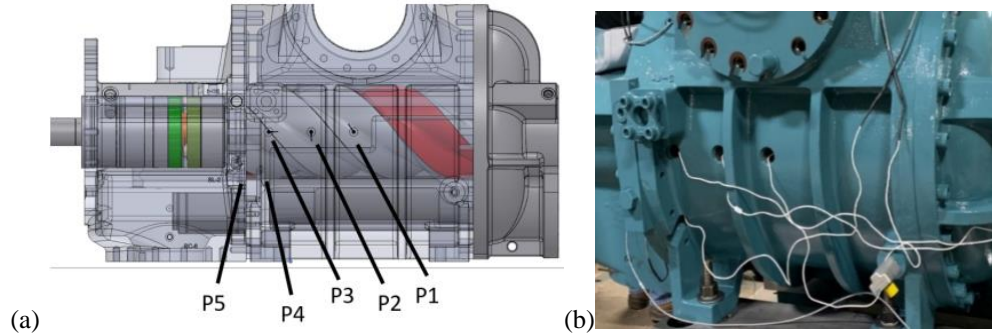


(a)                                                                 (b)
**Figure 1 – Location of placement of pressure transducers: a) CAD model; b) actual compressor.**

As for the load cells, a set of three compression load cells were installed on the discharge end of each of the male and female rotors to measure axial forces on the bearings (Salts *et al.*, 2019*)*. The load cells are mounted 120° apart from each other around the shaft and each set of load cells is placed under a spring pre-load such that they can measure forces in both the positive and negative direction. Specialized compression fittings have also been installed for the signal wires as the device itself is mounted inside.

The data from the sensors contained a certain amount of noise. To obtain cleaner data, a signal conditioner with the correct filtering settings was necessary. Recording the static readings of both pressure transducers and load cells before testing will also provide correct offset values for post-processing. Table 3 lists all the different sensors used within the experiment, their types, and uncertainties.

**Table 3: Summary of all sensors used and their properties**

| Measurement | Type | Accuracy |
|---|---|---|
| Dynamic Pressure | KULITE XTEL-190SM | ±0.5% FSO (Max.) |
| Axial Force | Tacsis XLCH–005T-TS | ±0.25% BFSL |
| Torque Meter | Lebow 1807-100K | ±0.1% FS |
| Optical Tachometer | SPSR-115/230, 6150-020 | |

## 4. DATA PROCESSING

As described previously, instantaneous data of the compression process is collected using five dynamic pressure transducers. It is necessary that the data from these pressure transducers are processed into a single pressure curve as a function of the rotation and volume increase. Therefore, the pressure traces must be aligned with the rotation and the working process. Developing an indicator diagram from pressure transducer data involves the following main steps:

- Combine the pressure sensor data into one pressure continuous pressure vs crank angle curve
- Compare with analytically developed volume vs crank angle curve
- Overlay pressure and volume curves to form indicator diagram
- Compute the areas with integration methods

### 4.1 Creating pressure vs crank angle curve

The five pressure transducers sample data based on a specific sampling rate. The data collected in a period depends on the transducer sampling rate and the RPM as explained previously. The transducers used in the experiment sample at a rate of 51,200 Hz. To sample exactly one period, the crank angle period $\Delta$, over one lobe is given by the relation:

$$\Delta = 51{,}200 * \beta / \left(RPM * \frac{360\ deg/rev}{60\ s/min}\right) \tag{10}$$

where $\beta$ is angle subtended by one lobe in the male rotor.

Figure 2 describes the process where the pressure data from the transducers are overlayed according to the calculated period. The pressure transducers are strategically placed around the rotor such that the pressure curves from the transducers slightly overlap each other. The overlap between the pressure transducers is averaged to develop a smoother, continuous curve. The smoother curve is curve fit using a spline fit.
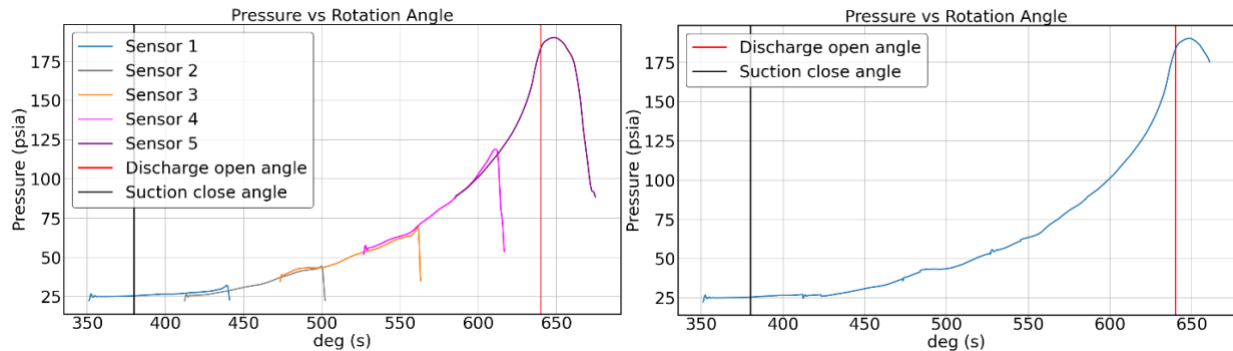


**Figure 2 – Stages of pressure curve processing (from left to right)**

### 4.2 Compression chamber volume curve

The volume vs crank angle curve is analytically developed by mapping the rotor profiles into a 3D domain and wrapping it across the length of the rotor. The exact procedure is explained in Wu and Tran (2016). The loading and volume ratio configurations modify the volume curve and lead to early discharge or delayed suction. Therefore, the discharge angle changes with different loading and is a function of slide valve position as described in Equation 11.

$$\theta_{suc} = 325 \cdot \left(\frac{SV_{pos}}{26.74}\right) + 104\ ;\ \theta_{dis} = 325 \cdot \left(\frac{SV_{pos}+15.38}{26.74}\right) + 325 \tag{11}$$

where $\theta_{dis}$ and $\theta_{suc}$ are angle of discharge open and angle of suction close respectively. $SV_{pos}$ stands for the position of slide valve in inches. The numbers are derived based on geometric parameters such as wrap angle, rotor length and rotor lead. These angles are used to predict the phase during which the compression process occurs. This is useful to segregate the pressure and volume vs crank angle curves into different sections of the indicator diagram as described in the next section.

### 4.3 Construction of indicator diagram

Once the volume curve and the suction/discharge angles are computed, the pressure and volume vs crank angle curves are combined. To achieve this, the phases of the indicator diagram: compression, suction, discharge must be separated from each other according to the start and end crank angles for each phase. The start and end angles of the suction, compression and discharge phases are from 0 to $\theta_{suc}$, $\theta_{suc}$ to $\theta_{dis}$, $\theta_{dis}$ to angle of end housing respectively. These are compartmentalized from the main pressure and volume vs crank angle curves and give rise to three different sections. These sections are independently processed using a spline fit. These are then combined to produce the indicator diagram.

The ideal curve is estimated based on the suction and discharge volumes and considering that the product of pressure and volume at the suction and discharge raised to the polytropic coefficient $\gamma$ is equal, the ideal curve polytropic coefficient can also be computed. These are compared with the experimental curves and the losses for each of the three phases are computed according to the relations previously described in Section 2.3.
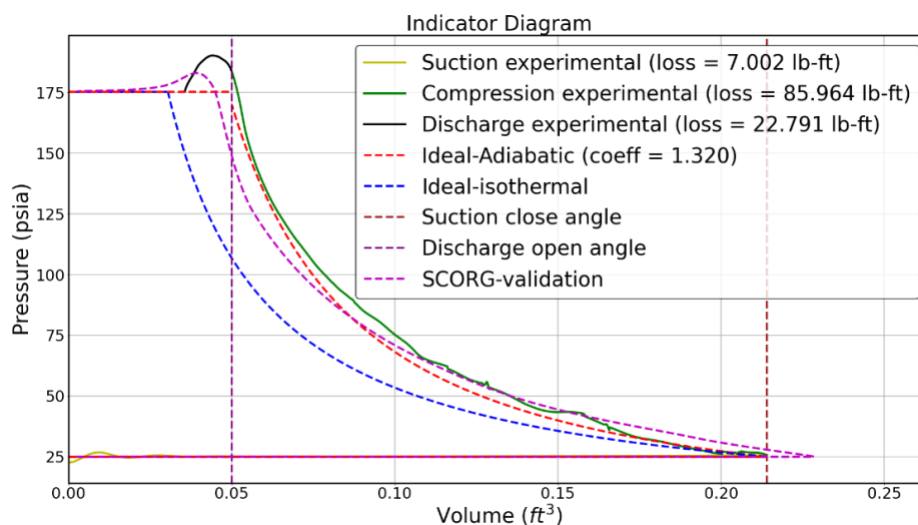
**Figure 3 – Indicator diagram with SCORG validation (Test #2)**

# 5. RESULTS AND DISCUSSION

The experimental indicator diagram is validated using a numerically generated indicator diagram. The experimental and numerical process agree within an acceptable error percentage. A comparison of suction, discharge, and compression losses along with the specific indicated power for various full and part load conditions is presented in this section. This section also discusses how certain conditions sacrifice performance and compromises isentropic, volumetric, polytropic and mechanical efficiencies.

## 5.1 Indicator diagram validation

The experimentally obtained indicator diagrams were validated using a numerically obtained indicator diagram from the software SCORG (Analysis, PDM 2022). The software takes in the male and female rotor profile coordinates and geometrically performs various thermodynamic, force calculations including the evaluation of indicator diagrams. This software has been peer reviewed extensively and is an established software in the screw machine industry. From Figure 3, it can be concluded that the numerical indicator diagram obtained through the SCORG model presents a very good approximation to the experimental data. However, the SCORG model has a slightly larger displacement volume, which leads to a higher maximum volume at suction.

Table 4 compares various geometric and thermodynamic values obtained theoretically against that obtained through the experimental indicator diagram for test #2. The geometrical parameter displacement volume agrees within 1.11% of theoretical value. With the close estimation of the displacement volume, it can be concluded that the volume curves obtained through SCORG and that is geometrically obtained agree within reasonable error. At the same test conditions of suction, discharge pressure, volume ratio and rotational speed; the indicated power obtained experimentally agrees within 0.9% and the shaft power agrees within 2.1%. The same can be said about the flow conditions as the actual gas mass flow rate agrees within 3.9% with equal volumetric efficiency. The SCORG model therefore validates the experimentally obtained indicator diagram within reasonable tolerances.

**Table 4: Comparison of theoretical and experimental predictions for Test #2**

| | Indicated power ($hp$) | Displacement volume $\left(\frac{ft^3}{rev}\right)$ | Shaft power ($hp$) | Theoretical gas mass flow rate (lbm/min) | Actual gas mass flow rate (lbm/min) | Volumetric efficiency (%) |
|---|---|---|---|---|---|---|
| **Experiment** | 434.0 | 0.904 | 482.19 | 195.33 | 175.8 | 90.0 |
| **SCORG** | 430.1 | 0.914 | 492.54 | 202.66 | 182.6 | 90.3 |
| **Error (%)** | 0.9 | 1.11 | 2.1 | 3.75 | 3.9 | 0.30 |

**5.2 Indicator diagram losses**

The procedure explained in earlier sections was used to compute indicated work losses for all the test conditions. From Figure 4, it can be said that the highest indicated power comes from test #20 and #3 in 1800 and 3600 RPM cases respectively. These two cases pertain to the volume ratio of 2. Therefore, it can be concluded that despite having lower polytropic adiabatic losses, as compared to the volume ratios of 4, these cases perform poorly as they require a lot of indicated work to compress to the same discharge pressure at a much lower volume ratio and a much higher polytropic coefficient. Further, by comparing #13, #17 and #18 on Figure 4a), it can also be concluded that part load conditions perform better than 100% load cases. This is the motivation for slide valve part load modulation for screw compressor used in different applications. The lower the load, the lower the power input. It can also be concluded that higher RPM cases absorb more power than the ones that operate on 1800 RPM. This can be due to the simple fact that the rotor torque power is directly proportional to the rotational speed. However, higher rotational speeds lead to higher mass flow rate through the refrigeration circuit and this is a tradeoff for the higher power input.

The indicated loss is obtained by comparing indicated work with the ideal polytropic compression curves. Figure 5a) depicts these losses (in horsepower) endured during the compression process through the histogram. Negative losses represent heat loss to the surroundings as it consumes lower work than the adiabatic curve whereas positive losses represent heat input during the compression process. Figure 5b) represents mechanical and isothermal efficiencies as a percentage.
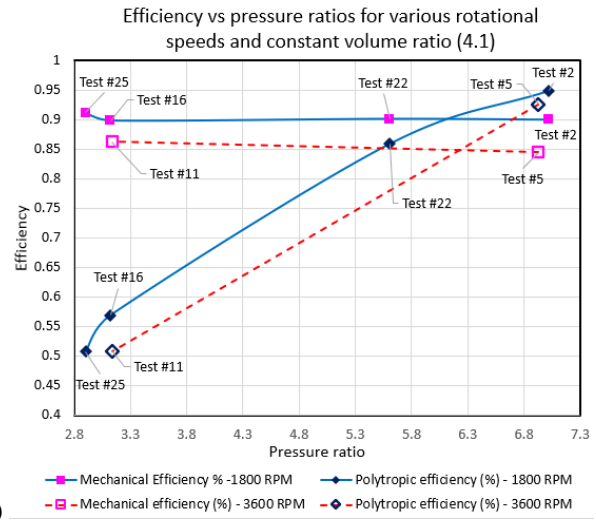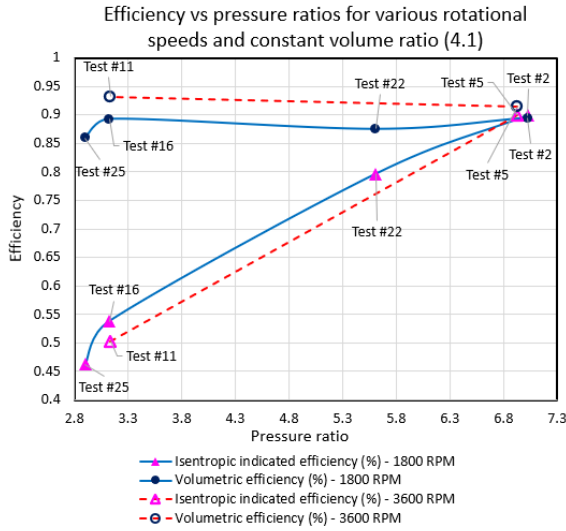


(a)

(b)
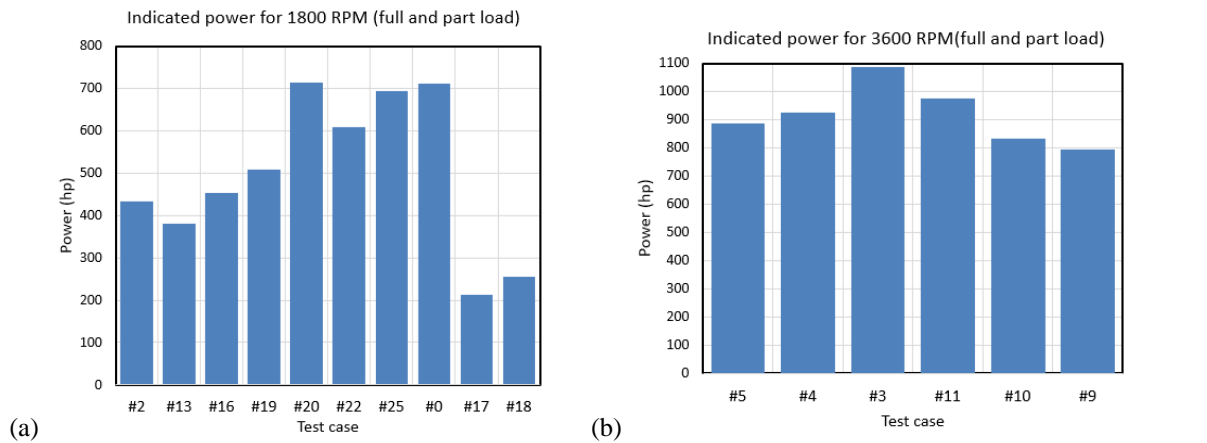
**Figure 4 – Histogram with experimental indicated power for cases with 100% load and a) 1800 RPM; b) 3600 RPM**
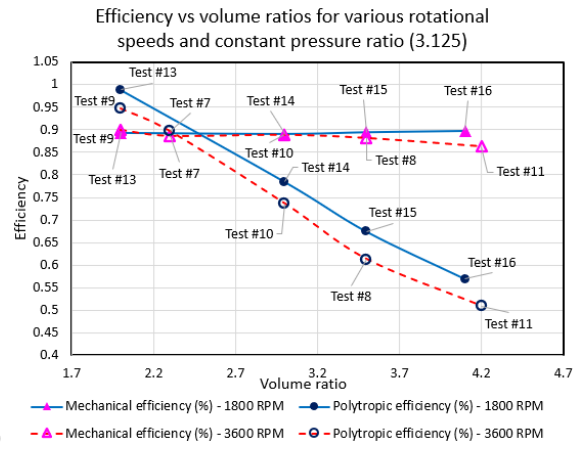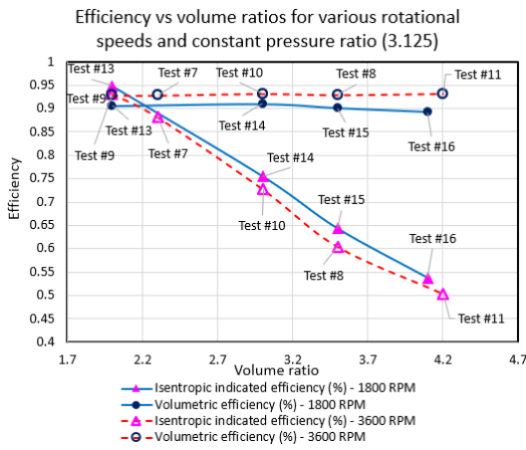


(a)

(b)
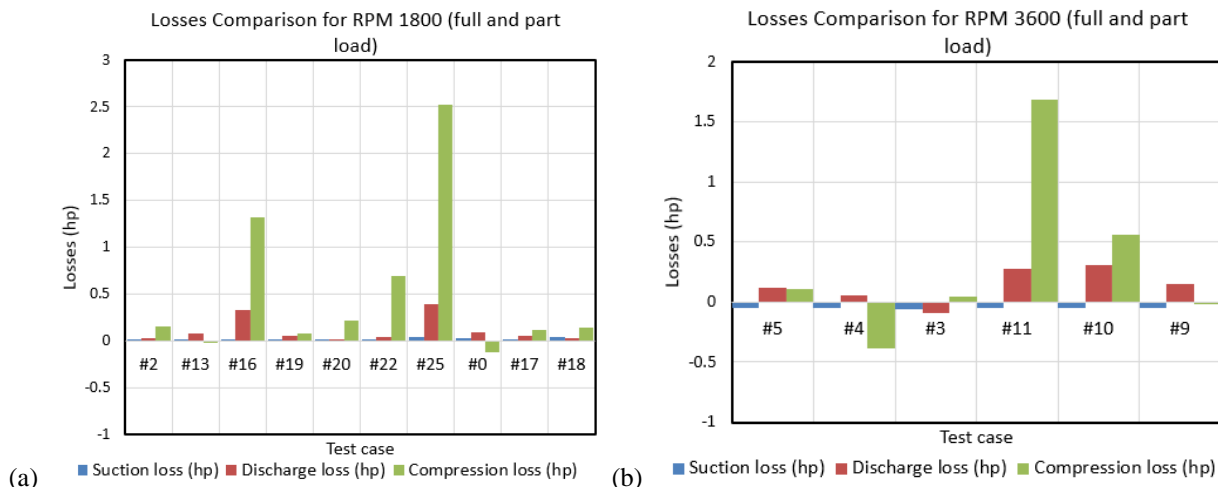
**Figure 5 – Histogram with suction, discharge, and compression loss in horsepower for cases with 100% load and a) 1800 RPM; b) 3600 RPM**

**Figure 6 – Line plot indicating trend of a) isentropic indicated and volumetric efficiencies; b) Mechanical and polytropic efficiencies over various pressure ratios at a constant volume ratio**
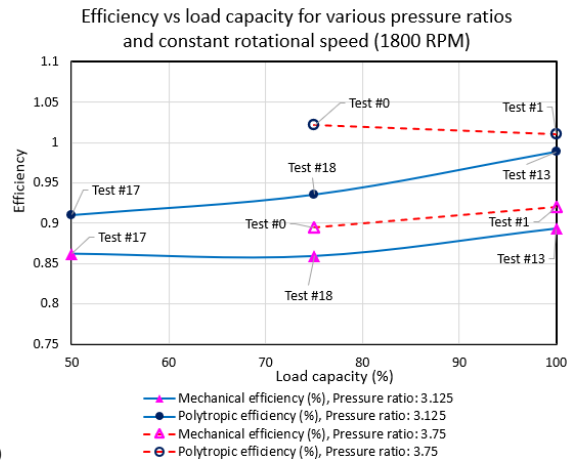


**Figure 7 – Line plot indicating trend of a) isentropic indicated and volumetric efficiencies; b) Mechanical and polytropic efficiencies over various volume ratios at a constant pressure ratio**
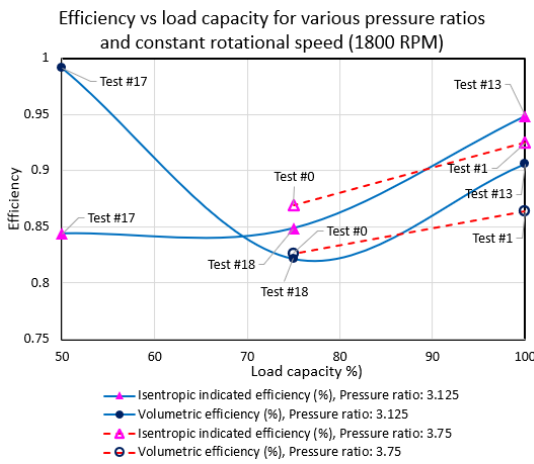


**Figure 8 – Line plot indicating trend of a) isentropic indicated and volumetric efficiencies; b) Mechanical and polytropic efficiencies for part load conditions**

Figures 6, 7 and 8 outline the variation of isentropic, volumetric, mechanical and polytropic efficiencies according to various pressure, volume ratios and part load conditions. Figures 6 and 7 display a clearly observable trend for the isentropic and polytropic efficiencies. It can be said that the isentropic and polytropic efficiencies increase with increase in pressure ratios but decrease with increasing volume ratios. The losses can be corroborated by comparing test #2 with #11 and #16 with #5 for varying pressure ratios or test #16 with #13 and #11 with #9 for varying volume ratios on Figure 7. From the plots, it can also be said that increasing rotational speeds would create more losses and hence lower isentropic and polytropic efficiencies for 3,600RPM compared to 1,800RPM. Throughout all the variations, the mechanical and volumetric efficiencies however remain consistent without much variation. This indicates that the clearance between the rotors is very tight and there is very minimal leakage losses. It also indicates that the bearing losses are very minimal leading to low frictional losses in all the cases. It can also be concluded that the volumetric and mechanical efficiencies do not have much dependance on the operating conditions for this compressor design due to modulation control mechanisms, but are primarily dependent on the geometrical setup.

For part load conditions (Figure 8), isentropic and polytropic efficiencies increase with increasing load capacity. However, this variation is not very significant. Depending on the needed capacity in a refrigeration circuit, part load modulation may or may not be required. In a realistic scenario, pressure ratios cannot be changed and are a fixed number, however volume ratio can be changed. As part load configurations lead to lower compressor power, part load configurations are desirable as long as the desired capacity is achievable with the reduced mass flow rates. For a fixed pressure ratio, losses within the compressor can be optimized by reducing volume ratios or through part-load modulation under specific circumstances.

## 5. CONCLUSIONS

In this paper, a comprehensive experimental and data processing procedure has been presented and validated. Five pressure transducers, six axial force sensors and one torque cell sensor are used in the experiment. The pressure data in the sensors was processed to produce a single pressure-crank angle curve, which was compared with the volume-crank angle curve to produce the indicator diagrams. The experiment consisted of 26 test conditions including various suction/discharge pressures and volume ratios at two different rotational speeds including full and part load conditions. The experimental indicator diagram was validated with a theoretical approach in SCORG, and the indicated power was within 10%. Through further observation of the indicator diagram losses, it was concluded that the higher-pressure ratios and lower volume ratios leads to lower adiabatic losses and the compression process is more isentropic. Decreasing load capacity leads to lower indicated power usage and is the motivation for part load modulation in twin-screw compressors. It was also concluded that the higher rotational speeds require higher indicated work and therefore higher losses and lower efficiencies. Volumetric and mechanical efficiencies however remain consistent through the varying operating conditions, and this shows that there are very limited frictional and volumetric losses. It can also be concluded that volumetric and mechanical efficiencies are not dependent on operating conditions but are dependent on the geometrical setup. In a real-world scenario with fixed pressure ratios, compressor losses can be minimized by lowering volume ratios or through part load modulation under some circumstances. Further investigation of the losses can be done, and a compressor map can be generated.

## NOMENCLATURE

| | | |
|---|---|---|
| $W_{loss}$ | loss in work | $lb - ft$ |
| $P$ | theoretical pressure | $psia$ |
| $V$ | Volume | $ft^3$ |
| $W_{\text{ind}}$ | indicated work | $lb - ft$ |
| $\dot{W}$ | power | $hp$ |
| $\dot{m}_{\text{suc}}$ | experimental suction mass flow rate | $lbm/min$ |
| $\rho_{suc}$ | suction density | $lbm/ft^3$ |
| $R$ | gas constant for nitrogen | $(ft - lb)/(lbm\ Rankine)$ |
| $T_{suc}$ | suction temperature | $Rankine$ |
| $N_1$ | male rotor rotational speed | $RPM$ |
| $z_1$ | number of male rotor lobes | $-$ |
| $\eta$ | efficiency | $-$ |
| $\gamma$ | polytropic coefficient | $-$ |
| $\beta$ | rotors wrap angle | $deg$ |

| Δ | crank angle period | | – |
|---|---|---|---|
| θ | crank angle | | *deg* |
| $SV_{pos}$ | slide valve position | | *in* |

**Subscript**

| comp | compressor | mech | mechanical |
|---|---|---|---|
| dis | discharge | pos | position |
| exp | experimental | shaft | shaft |
| isen | isentropic | suc | suction |
| ind | indicated | poly | polytropic |
| max | maximum | pos | position |
| chamber | working chamber | vol | volumetric |

# REFERENCES

Haugland, K., (1990). "Pressure Indication of Twin Screw Compressor". International Compressor Engineering Conference. Paper 735. https://docs.lib.purdue.edu/icec/735

Hou F., Zhao Z., Yu Z., Xing Z. (2017). Experimental study of the axial force on the rotors in a twin-screw refrigeration compressor. International Journal of refrigeration, 75, 155-163. DOI:http://dx.doi.org/10.1016/j.ijrefrig.2017.01.002

Huagen, W., Ziwen, X., & Pengcheng, S. (2004). Theoretical and experimental study on indicator diagram of twin screw refrigeration compressor. International Journal of Refrigeration, 27(4), 331–338. https://doi.org/10.1016/j.ijrefrig.2004.01.004

Jonsson, S. (1991). Performance simulations of twin-screw compressors with economizer. International Journal of Refrigeration, 14(6), 345-350. https://doi.org/10.1016/0140-7007(91)90031-B

Miyoshi, K. (1992). Analysis of Screw Compressor Performance Based on Indicator Diagrams. International Compressor Engineering Conference. Paper 815. https://docs.lib.purdue.edu/icec/815

PDM Analysis, (2022). SCORG. Link: https://pdmanalysis.co.uk/scorg/

Salts, N., Ziviani, D., & Groll, E. A. (2019). Application of a generalized compressor modeling framework for simulating an oil-injected twin-screw compressor. IOP Conference Series: Materials Science and Engineering, 604(1), 012009. https://doi.org/10.1088/1757-899x/604/1/012009

Seshaiah, N., Sahoo, R. K., & Sarangi, S. K. (2010). Theoretical and experimental studies on oil injected twin-screw air compressor when compressing different light and heavy gases. Applied Thermal Engineering, 30(4), 327–339. https://doi.org/10.1016/j.applthermaleng.2009.09.010

Stošic, N., Milutinović, L., Hanjalić, K., & Kovačević, A. (1992). Investigation of the influence of oil injection upon the screw compressor working process. International Journal of Refrigeration, 15(4), 206–220. https://doi.org/10.1016/0140-7007(92)90051-u

Sun, S., Xing, Z., Li, Y., Su, P. C., & Chen, W. (2021). Experimental investigation on twin screw refrigeration compressor with different capacity control methods. International Journal of Refrigeration, 130, 370–381. https://doi.org/10.1016/j.ijrefrig.2021.04.027

Wu, H., Peng, X., Xing, Z., & Shu, P. (2004). Experimental study on P–V indicator diagrams of twin-screw refrigeration compressor with economizer. Applied Thermal Engineering, 24(10), 1491–1500. https://doi.org/10.1016/j.applthermaleng.2003.11.015

Wu, Y. R. and Tran, V. T. (2016). Dynamic response prediction of a twin-screw compressor with gas-induced cyclic loads based on multi-body dynamics. International Journal of Refrigeration, 65, 111–128. https://doi.org/10.1016/j.ijrefrig.2015.12.002

## ACKNOWLEDGEMENT

## APPENDIX A

**Table A1a: Test matrix**

| Test | 0 | 1 | 3 | 4 | 5 | 6 | 7 | 8 | 9 |
|------|-----|-----|-----|-----|-----|-----|-----|-----|-----|
| RPM | 1800 | 1800 | 3600 | 3600 | 3600 | 3600 | 3600 | 3600 | 3600 |
| $P_{SUC}$ (psi) | 60 | 60 | 25 | 25 | 25 | 25 | 40 | 40 | 40 |
| $P_{DIS}$ (psi) | 225 | 225 | 175 | 175 | 175 | 175 | 125 | 125 | 125 |
| Volume Ratio | 2 | 2 | 2 | 3 | 4.1 | 4 | 2.3 | 3.5 | 2 |
| Load | 100 | 75 | 100 | 100 | 100 | 100 | 100 | 100 | 100 |
| $\dot{m}_{suc}$ (lbm/min) | 414.643 | 293.149 | 355.52 | 364.211 | 364.782 | 366.27 | 589.737 | 587.59 | 586.796 |
| $\dot{m}_{dis}$ (lbm/min) | 417.504 | 296.164 | 359.87 | 368.413 | 368.646 | 370.19 | 591.434 | 587.839 | 588.376 |

**Table A1b: Test matrix (continued)**

| Test | 10 | 11 | 12 | 13 | 14 | 15 | 16 | 17 |
|------|-----|-----|-----|-----|-----|-----|-----|-----|
| RPM | 3600 | 3600 | 3600 | 1800 | 1800 | 1800 | 1800 | 1800 |
| $P_{SUC}$ (psi) | 40 | 40 | 25 | 40 | 40 | 40 | 40 | 40 |
| $P_{DIS}$ (psi) | 125 | 125 | 175 | 125 | 125 | 125 | 125 | 125 |
| Volume Ratio | 3 | 4.1 | 3.5 | 2 | 3 | 3.5 | 4.1 | 2.3 |
| Load | 100 | 100 | 100 | 100 | 100 | 100 | 100 | 50 |
| $\dot{m}_{suc}$ (lbm/min) | 590.606 | 582.096 | 364.519 | 288.62 | 291.967 | 288.547 | 284.428 | 157.271 |
| $\dot{m}_{dis}$ (lbm/min) | 591.666 | 583.587 | 368.518 | 290.977 | 294.289 | 290.949 | 286.57 | 159.926 |

**Table A1c: Test matrix (continued)**

| Test | 18 | 19 | 20 | 21 | 22 | 23 | 24 | 25 | 26 |
|------|-----|-----|-----|-----|-----|-----|-----|-----|-----|
| RPM | 1800 | 1800 | 1800 | 1800 | 1800 | 1800 | 1800 | 1800 | 1800 |
| $P_{SUC}$ (psi) | 40 | 40 | 40 | 40 | 40 | 60 | 60 | 60 | 60 |
| $P_{DIS}$ (psi) | 125 | 175 | 225 | 225 | 225 | 175 | 175 | 175 | 175 |
| Volume Ratio | 2.3 | 2.7 | 2 | 2.3 | 4.1 | 2 | 3.1 | 4.1 | 2.5 |
| Load | 75 | 100 | 100 | 100 | 100 | 100 | 100 | 100 | 100 |
| $\dot{m}_{suc}$ (lbm/min) | 194.928 | 280.035 | 266.646 | 272.977 | 275.999 | 420.747 | 421.28 | 412.292 | 428.081 |
| $\dot{m}_{dis}$ (lbm/min) | 197.482 | 283.653 | 270.095 | 276.819 | 279.003 | 426.172 | 424.385 | 419.349 | 431.331 |